Computer Methods in Biomechanics and Biomedical Engineering
Vol. 00, No. 00, January 2012, 1–19

Original Article

A non-linear dynamic finite element approach for simulating muscular hydrostats

V. Vavourakis[a*], A. Kazakidi[a], D.P. Tsakiris[a] and J.A. Ekaterinaris[b,c]

[a]*Institute of Computer Science, Foundation for Research and Technology-Hellas, Heraklion, Crete 71110, Greece*; [b]*Department of Mechanical and Aerospace Engineering, University of Patras, Rio 26500, Greece*; [c]*Institute of Applied and Computational Mathematics, Foundation for Research and Technology-Hellas, Heraklion, Crete 71110, Greece*

(*Received 00 Month 200x; final version received 00 Month 200x*)

An implicit non-linear finite element model for simulating biological muscle mechanics is developed. The numerical method is suitable for dynamic simulations of three-dimensional non-linear nearly incompressible hyperelastic materials that undergo large displacements and deformations. These features characterize human and animal muscles, which consist of fibers and connective tissues. It can be assumed that the stress distribution inside muscles is the superposition of stresses along the fibers and the connective tissues. The mechanical behavior of the surrounding tissues is determined by adopting a Mooney-Rivlin constitutive model, while the mechanical description of fibers is considered to be the sum of active and passive stresses. Due to the non-linear nature of the problem, determination of the Jacobian matrix is performed, in order to utilize the standard Newton-Raphson iterative procedure, and time integration is accomplished via the implicit Newmark method. The proposed methodology is validated by comparing our numerical results with experimental measurements and other numerical results. Numerical simulations for large deflections of octopus arm muscles are carried out with our open-source finite element software.

Keywords: FEM; large deformation; biological muscles; octopus

1. Introduction

Muscles can be considered the bio-materials that in contrast with other biological tissues deform voluntarily. To this point, simulation of muscles behavior has been the subject of many research activities. However, due to muscles' complex mechanical nature (Fung 1981) and their ability to undergo large deformations, numerical simulation of such problems requires utilization of a non-linear approach. Finite element discretization is the method of choice for the numerical solution of these problems.

Amongst the pioneering works in skeletal muscles' computational mechanics through the finite element method (FEM), Kojic et al. (1998) proposed a numerical algorithm for the determination of muscle response, where Hill's three-element model (Hill 1938) was used for the mechanical description of fibers. They accounted for non-linear force-displacement relation and change of geometrical shape; however, their major simplification was that passive behavior of the muscle is linear elastic and isotropic, while no incompressibility was taken into account. Martins

*Corresponding author. Present Address: Department of Civil and Environmental Engineering, University of Cyprus, Nicosia 1678, Cyprus. Tel.:+357 22892232. Email: vasvav@ucy.ac.cy

ISSN: 1741-5977 print/ISSN 1741-5985 online

DOI: 10.1080/1741597YYxxxxxxxx
http://www.informaworld.com

et al. (1998) developed a 3D FE platform for the simulation of skeletal muscles, in which the constitutive relation adopted is a generalization of the model proposed by Humphrey & Yin (1987), being compatible with the passive and active behavior of skeletal muscles of Zajac (1989). Johansson et al. (2000) proposed a FEM for simulating muscles behavior based on non-linear continuum mechanics, where contractile active and passive properties of skeletal muscles were considered and incompressibility is fully incorporated. On the other hand, Oomens et al. (2003) proposed a FE approach, where physiological reasoning and 'cross-bridge' kinetics via a two-state Huxley model (Huxley 1957) was adopted, for the mechanical behavior investigation of a tibialis anterior of a rat. Furthermore, Fernandez et al. (2005) presented a FE muscle modeling framework that relates the mechanical response of the rectus femoris muscle to tissue level properties, with the capability of linking to the cellular level.

Recently, Liang et al. (2006), based upon the approach of Van Leeuwen & Kier (1997), incorporated the governing equations for a muscle element into a commercial general-purpose explicit FE program. Their scheme is promising because it can simulate complex dynamic muscular behaviors but it suffers from the small time-step restriction, required by numerical stability considerations. In the same year, Martins et al. (2006) introduced a multiplicative split of the fiber stretch into contractile and elastic stretches, where they considered the simultaneous presence of the series elastic element, the dependence of the contractile stress on the strain rate and an activation level function. Röhrle & Pullan (2007) also presented a 3D dynamic Galerkin FEM framework of an anatomically realistic model of the human masseter muscles and associated bones.

Further developments in muscle modeling presented by Tang et al. (2007), where Hill's muscle theory coupled with fatigue was proposed to describe the mechanical behavior of skeletal muscles. They compared the proposed FE technique with the experimental results on a frog muscle, capturing the real-time shape change due to fatigue. Stojanovic et al. (2007) proposed an extension of Hill's model of Kojic et al. (1998). It was presented a model consisting of different types of sarcomere coupled in parallel with the connective tissues, where each sarcomere was modeled by one non-linear elastic element connected in series with one non-linear contractile element. Tang et al. (2009) presented a 3D FE model, developed to simulate active and passive non-linear mechanical behavior of muscle during lengthening or shortening. The constitutive relation of the muscle was determined by using a strain energy approach, while active contraction behavior of the muscle fiber was modeled through Hill's three-element muscle concept. More recently, Lu et al. (2010) developed a visco-hyperelastic model for skeletal muscles, where the constitutive relation was based on the definition of a Helmholtz energy-free function, involving fourteen material parameters.

The literature survey demonstrates that active muscle behavior has been modeled with two main approaches: Hill-type and Huxley-type based models. However, in the present paper, it is assumed that the nominal tensile stress in muscles is derived from the maximum isometric stress, the normalized active level function, the velocity dependence function, the filamentary overlap function and a passive component, similar to the approach of Van Leeuwen (1991). This rather simple approach is also refered as the additive split of active and passive stresses, which is consistent with Hill's three-element model muscle representation (Van Leeuwen & Kier 1997).

The present work was motivated by the OCTOPUS IP[1] project that aims to

[1] http://www.octopusproject.eu/index.html

the design and development of octopus-like robotic arms. In connection to this objective, the development of a robust and efficient tool for the 3D kinematic and dynamic modeling of the octopus musculature was a need. As it will be demonstrated in the numerical examples section, this paper is a preliminary study on the biomechanical aspects (e.g. level and pattern of muscles activation) of the muscular hydrostats behavior via the reproduction of primitive octopus arm maneuvers, like bending and reaching.

2. Numerical method

Consider a non-linear, homogeneous elastic continuous medium of volume ${}_0V$ and surface ${}_0S$ in its unloaded state that undergoes large deformations. The volume and bounding surface of the body in its current (deformed) stated is denoted as ${}^tV$ and ${}^tS$, respectively.

A fundamental quantity for the description of deformation in non-linear continuum mechanics is the deformation gradient, which may be expressed in terms of the current coordinates ${}^tx_i$ of a material point or the displacements u_i through the relation: $F_{ij} = \partial\, {}^tx_i / \partial\, {}_0x_j = \delta_{ij} + \partial u_i / \partial\, {}_0x_j$, where δ_{ij} is the Kronecker delta. In addition, proper stress and strain measures are needed that relate these quantities with the currently-deformed state of the solid body. Such measures are the Cauchy stresses σ_{ij} and the left Cauchy-Green deformation tensor $B_{ij} = F_{in}F_{jn}$.

Using quantities related to the current configuration, the equilibrium equations for a solid subject to finite deformation are nearly identical to those for small deformation analysis. The local equilibrium equation is obtained as a force balance on a small differential volume of the deformed solid

$$\frac{\partial \sigma_{ij}}{\partial\, {}^tx_j} = {}^t\rho\, \ddot{u}_i\,, \tag{1}$$

where body forces have been neglected and ${}^t\rho$ is the material density.

Proper boundary conditions are considered for well-posing this problem. Prescribed displacements are assumed on ${}_0S_U$ and corresponding prescribed tractions are assumed on ${}_0S_T$, with ${}_0S = {}_0S_U \cup {}_0S_T$.

Muscles are composite materials comprising of connective tissues and bio-bluids, and muscle fibers. Hence, it can be safely assumed that the stress distribution inside an element of the muscle is the superposition of stresses in the connective tissues and the fibers, i.e. $\sigma_{ij} = \sigma_{ij}^{(ct)} + \sigma_{ij}^{(f)}$, where the superscripts 'ct' and 'f' denote the connective tissue and fibrous part, respectively.

2.1 Connective tissues description

In most cases, biological tissues are best described through a hyperelastic Mooney-Rivlin (Mooney 1940) constitutive relation, where the calculation of the Cauchy stress tensor can be obtained by differentiation of a stored energy function $W(I_1, I_2, J)$ with respect to deformation as

$$\sigma_{ij} = \frac{2}{J}\frac{\partial W}{\partial C_{ij}}\,, \tag{2}$$

where $C_{ij} = F_{ni}F_{nj}$ the right Cauchy-Green deformation tensor, $I_1 = \mathrm{tr}(B_{ij})$,

$I_2 = [I_1^2 - B_{kl}B_{lk}]/2$ and $J = \det(F_{ij})$.

However, rubber-like materials and biological tissues exhibit nearly or fully incompressible behavior, thus, the $J \approx 1$ constraint must be satisfied. Towards this end, the following modified invariants are introduced: $\bar{I}_1 = I_1 J^{-2/3}$ and $\bar{I}_2 = I_2 J^{-4/3}$ based on the modified deformation gradient tensor $\bar{F}_{ij} = F_{ij} J^{-1/3}$ (Zienkiewicz & Taylor 2005). Applying the chain differentiation rule in Eq. 2, the following analytic expression of the Cauchy stresses is obtained

$$\sigma_{ij}^{(ct)} = \frac{2}{J^{5/3}}\left(\frac{\partial \bar{W}}{\partial \bar{I}_1} + \bar{I}_1 \frac{\partial \bar{W}}{\partial \bar{I}_2}\right) B_{ij} - \frac{2}{J^{7/3}} \frac{\partial \bar{W}}{\partial \bar{I}_2} B_{im}B_{mj} - \frac{2}{3J}\left(\bar{I}_1 \frac{\partial \bar{W}}{\partial \bar{I}_1} + 2\bar{I}_2 \frac{\partial \bar{W}}{\partial \bar{I}_2}\right)\delta_{ij} + \frac{\partial \bar{W}}{\partial J}\delta_{ij}\,. \tag{3}$$

Substituting the modified generalized Mooney-Rivlin constitutive material relation: $\bar{W} = c_1(\bar{I}_1 - 3) + c_2(\bar{I}_2 - 3) + {}^{K}/_{2}(J-1)^2$ into Eq. 3, the analytic expression of the Cauchy stress tensor for the connective tissues is obtained as follows

$$\sigma_{ij}^{(ct)} = 2(c_1 + c_2\bar{I}_1)J^{-5/3}B_{ij} - 2c_2 J^{-7/3}B_{im}B_{mj} - \left[({}^{2}/_{3J})\,(c_1\bar{I}_1 + 2c_2\bar{I}_2) + K(1-J)\right]\delta_{ij}\,, \tag{4}$$

where c_1, c_2, are material constants and K the bulk modulus, which for the present analysis assumes high values so that incompressibility is enforced via this penalty-like term.

2.2 *Muscle fibers material description*

The main structural components of the muscular system that have active role are the muscle fibers. Due to their contractive properties the muscle contracts and causes muscle deformation. A muscle fiber comprises of parallel bundles of myofibrils, which in turn are divided longitudinally by the Z-discs into sarcomeres. However, a more detailed description of the muscular structure can be found in (Nigg & Herzog 1999).

Consider a uniquely-defined direction vector at every material point of the muscle along the fiber, denoted with $\hat{n}_i$, $\hat{m}_i$ at the undeformed and current configuration, respectively. The updated fiber orientation is obtained by: $\hat{m}_i = {}^{1}/_{\lambda}\,(F_{ij}\hat{n}_j)$, where $\lambda = \sqrt{\hat{n}_i C_{ij} \hat{n}_j}$ is the fiber stretch ratio.

The nominal strain is defined by the change of length divided by the reference length of the fiber and is given by: $\varepsilon_0^m = \lambda - 1$. Therefore, the corresponding volume preserving fiber strain tensor can be written as (Liang et al. 2006): $\varepsilon_{ij}^{(f)} = \varepsilon^m\,(3\hat{m}_i\hat{m}_j + \delta_{ij})\,/2$, while the corresponding Cauchy stress tensor has the form

$$\sigma_{ij}^{(f)} = \sigma^m\,\hat{m}_i\,\hat{m}_j\,, \tag{5}$$

where the nominal axial stress σ_0^m is defined in terms of the Cauchy true fiber stress: $\sigma^m = \sigma_0^m\,(\varepsilon_0^m + 1)$.

According to Van Leeuwen (1991), the fiber nominal axial stress in muscles is defined as the accumulation of passive $\sigma^{(pass)}$ and active axial stress. The latter part is considered to be the product of the maximum isometric stress $\sigma^{(max)}$ at

fiber optimum length, a normalized active state function $f^{(a)}(t)$ that describes the activation pattern, a force-length $f^{(l)}$ and a force-velocity function $f^{(v)}$ that relate the active muscle stress with ε_0^m, $\dot{\varepsilon}_0^m$, respectively,

$$\sigma_0^m = \sigma^{(pass)} + \sigma^{(max)}\, f^{(a)}\, f^{(l)}\, f^{(v)}\,. \tag{6}$$

The above assumption is based upon the sliding filament theory of Huxley (1957).

2.3 Finite element discretization

The balance Eq. 1 can be replaced by an equivalent principle of virtual work, which has to be in a form appropriate for finite deformations. The variational theorem for finite elasticity in the current configuration (Bowler 2009) reads

$$\delta\Pi = \int_{{}^tV} \delta v_i\; {}^t\rho\, \ddot{u}_i\, dV + \int_{{}^tV} \delta L_{ij}\, \sigma_{ij}\, dV - \int_{{}^tS_T} \delta v_i\, \bar{t}_i\, dS = 0\,, \tag{7}$$

where ${}^t\rho$ the current material density, $\bar{t}_i$ the prescribed tractions on ${}_0S_T$, δv_i an admissible velocity variation that satisfies the condition: $\delta v_i = 0$ on ${}_0S_U$, and δL_{ij} the virtual velocity gradient variation. It can be seen from Eq. 7 that the integrals are evaluated with respect to the current configuration. Therefore, proper transformations should be applied in order to convert the integrals into the undeformed configuration, since the initial shape of the solid is known. Such transformations are the following (Zienkiewicz & Taylor 2005): ${}_0\rho = J\,{}^t\rho$, $d\,{}^tx_i = F_{ij}\, d\,{}_0x_j$, $d\,{}^tS = J_\gamma\, d\,{}_0S$ and $d\,{}^tV = J\, d\,{}_0V$, where $J_\gamma = J\sqrt{\hat{n}_i\, B_{ij}^{-1}\hat{n}_j}$.

Due to the material and geometrical non-linearies arising to this problem, a proper linearization procedure is needed to facilitate further numerical implementation via the standard Newton-Raphson method. Linearizing Eq. 7 with respect to the unknown displacement field, and assuming a proper FE discretization, the final semi-discrete matrix form of the balance equation is obtained

$$M_{ij}^{(\alpha,\beta)}\ddot{u}_j^{(\beta)} + K_{ik}^{(\alpha,\beta)}\Delta u_k^{(\beta)} = R_i^{(\alpha)} - F_i^{(\alpha)}\,, \tag{8}$$

where

$$K_{ik}^{(\alpha,\beta)} = \int_{{}_0V}\left(\frac{\partial\sigma_{ij}}{\partial F_{km}}\, F_{lm} + \sigma_{ij}\delta_{kl}\right)\frac{\partial N^{(\alpha)}}{\partial {}^tx_j}\,\frac{\partial N^{(\beta)}}{\partial {}^tx_l}\, J\, dV + \int_{{}_0V}\sigma_{ij}\,\frac{\partial N^{(\alpha)}}{\partial {}^tx_k}\,\frac{\partial N^{(\beta)}}{\partial {}^tx_j}\, J\, dV\,,$$

$$M_{ij}^{(\alpha,\beta)} = {}_0\rho\int_{{}_0V}\delta_{ij}\, N^{(\alpha)}N^{(\beta)}dV\,,$$

$$R_i^{(\alpha)} = \int_{{}_0S_T} N^{(\alpha)}\,\bar{t}_i\, J_\gamma\, dS\,,\quad F_i^{(\alpha)} = \int_{{}_0V}\sigma_{ij}\,\frac{\partial N^{(\alpha)}}{\partial {}^tx_j}\, J\, dV\,.$$

In the above Jacobian matrix $K_{ij}^{(\alpha,\beta)}$ it is assumed that no follower external forces are present, where the first integral corresponds to the material tangent stiffness and the second one is called the geometric stiffness. Furthermore, the matrix $M_{ij}^{(\alpha,\beta)}$

accounts for the lumped mass contribution, while $R_i^{(\alpha)}$, $F_i^{(\alpha)}$ are the external and internal force contribution vectors, respectively. Further details on the linearization steps required as well as the calculation of the tangent stiffness tensor components are provided in the Appendix.

In the present study, the Newmark implicit method (Zienkiewicz & Taylor 2005) is used for the time advancement of the semi-discrete form of Eq. 8. Taking the successive procedure of Newton-Raphson iterations for each time-step until convergence is achieved, the transient analysis ends up to the desired time of dynamic observation of the non-linear system.

The numerical implementation of the finite element procedure –as presented above– for the simulation of the dynamic mechanical behavior of 3D muscles was carried out through our scalable C++ program. The project built utilizes available open-source numerical libraries, such as PETSc[1] (Balay et al. 2008) and libMesh[2] (Kirk et al. 2006).

3. Results

In this section, it is presented the dynamic simulation of the squid arm extension and of the frog gastrocnemius muscle contraction, in order to validate the proposed methodology. This will be achieved by comparing the obtained numerical results with experimental measurements and other numerical results that are available in the literature. In addition, various simulations of the octopus arm muscular hydrostat are presented, where different muscle groups activation and various activation patterns are performed, in order to enhance our understanding of the underlying muscle mechanics in the octopus arm maneuverability.

3.1 Dynamic squid arm extension

The first numerical example involves the dynamic extension of a squid arm during the strike to catch prey. The squid arm consists of an active stalk and a passive club, as depicted in Fig. 1(b), having 95 mm total length. For simplicity, the squid arm is modeled as a cylindrical body. The stalk composes of 15% longitudinal muscles having fiber orientation along the z-axis (represented by an outer 0.3 mm thickness layer), and an inner cylindrical core of transverse muscles of 3.4 mm radius (see Fig. 1(a)). The club is considered in the present analysis to have the same muscular structure as in the stalk but it is taken to behave passively. Detailed description of the squid musculature is given by Van Leeuwen & Kier (1997). The material properties of the muscle fibers and connective tissues are identical to the ones used by previous investigations (Johansson et al. 2000; Liang et al. 2006), while the applied activation signal for the current simulation is the following step time-function

$$f^{(a)} = \begin{cases} \left[\frac{1}{2}\left(1+\sin\left(\pi t/t_a - \pi/2\right)\right)\right]^{15}, & t \leqslant t_a \\ 1, & t > t_a \end{cases},$$

where the signal peak-value time is set $t_a = 40$ msec.

[1] http://www.mcs.anl.gov/petsc/petsc-as/
[2] http://libmesh.sourceforge.net/

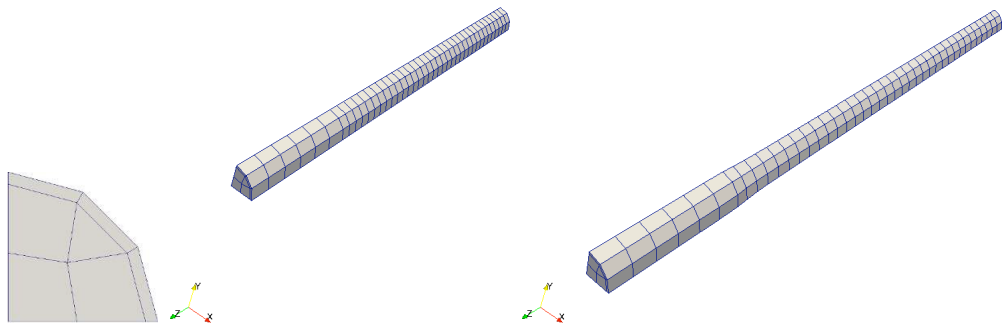

Figure 1. (a) Finite element discretization of the quarter cross-section of squid arm, with (b) initial (undeformed) configuration and (c) final (deformed) shape of the squid arm during the strike to catch prey simulation.

Due to symmetry, only one quadrant of the cylindrical arm is modeled and appropriate boundary conditions are applied to the symmetry planes; the surface on the root of the arm is restricted to move axially, while the rest of the surfaces are taken traction-free. Discretization is accomplished with the aid of the open-source mesh generator Gmsh (Geuzaine & Remacle 2009). The mesh consists of 246 eight-node hexahedral and 41 six-node triangular-base prism elements (see Fig. 1(b)).

As the activation signal $f^{(a)}$ increases, transverse muscles contract resulting in the axial arm deformation. In order to maintain constant volume, the radius of the arm decreases while length increases. After 45 msec of full activation, the passive tensile forces of the longitudinal muscles are greater than the contractile active forces of the transverse muscles. Thus, leading to extension deceleration and finally to maneuver termination. The final deformed squid arm is depicted in Fig. 1(c).

Fig. 2(a) shows the squid arm length growth in time. The FE numerical results, obtained by the current methodology (diagonal crosses), are compared with the experimental data (empty diamonds) of the squid arm extension and the corresponding 1D model simulations (solid line) obtained by Van Leeuwen & Kier (1997). In view of Fig. 2, it is observed that the FEM numerical results agree very well both qualitatively and quantitatively with those in (Van Leeuwen & Kier 1997). However, in Fig. 2(b) it can be noticed that a relatively lower arm-tip velocity is evaluated through the proposed analysis. It is interesting to note that similar behavior was observed by other FEM approaches (Johansson et al. 2000; Liang et al. 2006; Tang et al. 2009). In order to examine for the numerical scheme h-refinement convergence, the dynamic squid arm extension problem was solved for another two finer finite element discretizations. As expected, the obtained numerical results improved, resulting into less fluctuation behavior after 45 msec of full activation, while the evaluated tentacle length converged to the experimental measurement.

3.2 Frog gastrocnemius muscle

Next, the deformation of the frog gastrocnemius muscle subjected to activation under a constant tensile load along the muscle fiber direction is simulated. The muscle geometry assumed is provided in (Tang et al. 2007), while the material parameters are adopted from their successive work (Tang et al. 2009). In these studies, a Hill three-element model is utilized in order to describe the mechanical behavior of sceletal muscles. To this end, analytical evaluation of the Cauchy stress tensor and tangent stiffness tensor in the fiber and connective tissue level is performed, and

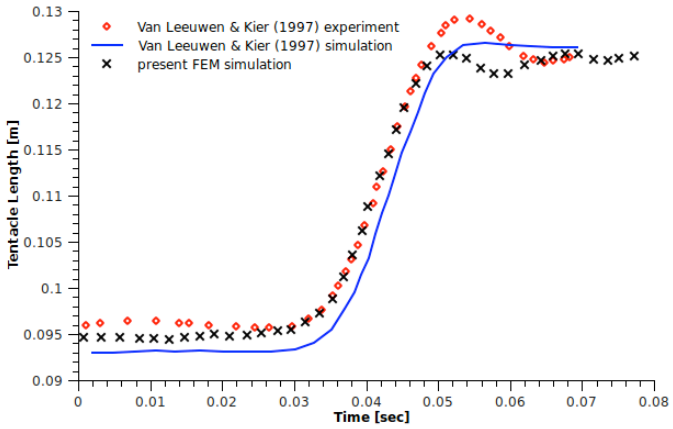

(a)

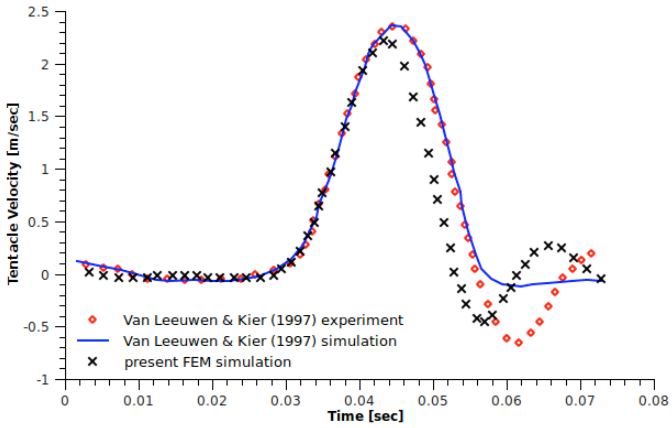

(b)

Figure 2. Comparison of experimental and simulation results of the squid (a) arm length and (b) arm-tip velocity profile.

presented in B. The activation load is identical to the one of Tang et al. (2009) and similar boundary conditions are considered. However, in the present simulation, muscles fatigue is not taken into account. In Fig. 3(a) the FE discretization of the frog gastrocnemius muscle –comprising of 480 eight-node hexahedral elements– is depicted. The fiber orientation is defined by the local z-axis of each finite element, which follows the fusiform muscle geometry. In Fig. 3(b) the final deformed body of the muscle is also shown.

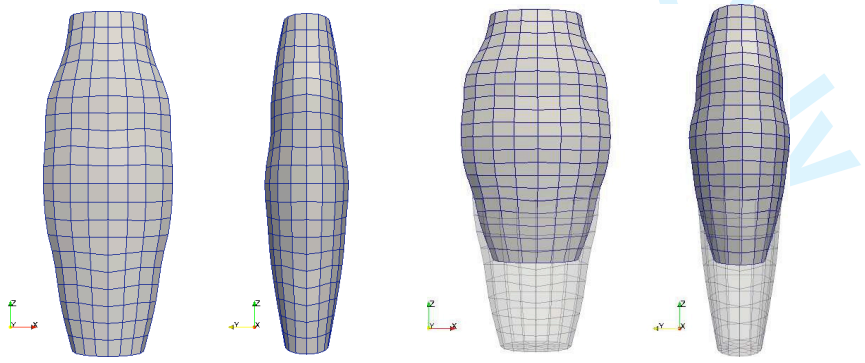

(a) *(b)*

Figure 3. (a) Finite element discretization of the undeformed frog muscle and (b) final deformed geometry.

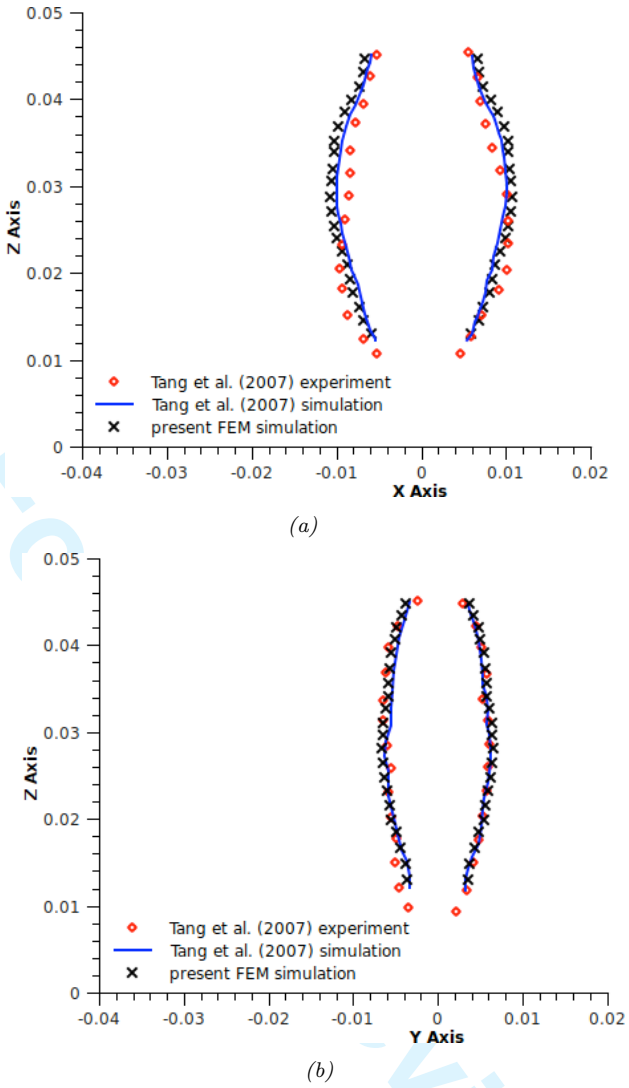

Figure 4. Deformed shape outline of the frog gastrocnemius muscle and comparison of the experimental and simulation results on the (a) x-z and (b) y-z planes.

In Fig. 4 comparison of the deformed shape outline of the frog muscle at maximum activation level on the x-z and y-z planes is shown. In this figure, the experimental results obtained by Tang et al. (2007) and their numerical results at the first activation circle, with the numerical results of the current FE procedure are compared. The numerical results in both FE approaches are in relatively close agreement to the experimental measurements.

3.3 Octopus muscular hydrostat dynamic simulations

Finally, a conical geometry of the octopus arm extending along the z-axis, being 10 cm long and having 1 cm root diameter, is considered. The arrangement of muscles in the octopus muscular hydrostat (Kier & Stella 2007) is very different compared to that of the squid arm, and is depicted in Fig. 5(a). The arm musculature consists mainly of longitudinal muscles (denoted with 'L' in Fig. 5(a)) that extend along the arm axial direction, and transverse muscles (denoted with 'T') that connect the external connective tissues with the longitudinal muscles and the axial nerve cord (denoted with 'N'). In addition, oblique muscles are present (denoted with 'O'), which are helically aligned fibers around the arm, thus, enabling

arm torsion. For the present analysis, oblique muscles are omitted, because their contribution to bending motion of the octopus arm is minor (Liang et al. 2006; Yekutieli et al. 2005). However, the lack of experimental data on the octopus muscular hydrostat material properties restricts us to utilize the corresponding ones of the squid, provided in (Van Leeuwen & Kier 1997). This assumption is based upon the fact that both molluscs are of the same class (cephalopoda), despite their arm different muscular structure.

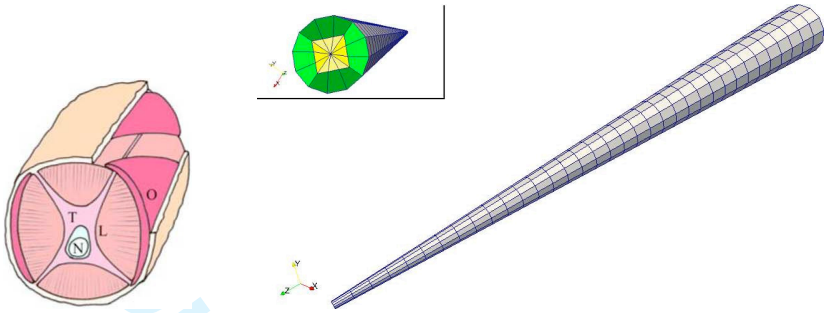

(a) (b)

Figure 5. (a) Diagram of the octopus arm showing the arrangement of muscle fibers and connective tissues. (b) Finite element discretization of the octopus arm and close-up view of the arm root on the top left of the subfigure.

The FE mesh of the octopus arm consists of 420 eight-node hexahedral and 420 six-node triangular-base prismatic elements, as seen in Fig. 5(b). On the top of the same figure it is depicted the two main muscular kinds of longitudinal and transverse muscles (shaded with different colours) considered in the octopus arm. Following Fig. 5(a), the longitudinal muscles are taken as four distinctive subregions (green-colour regions), thus, enabling them for separate activation; while the transverse muscles are located in the core of the idealized conical octopus arm (yellow-colour regions).

The wet area of the arm is considered traction-free, while the root of the arm is allowed to move on the x-y plane and is fixed at the origin point $(0, 0, 0)$. The applied activation signal for the current simulation is a step function, defined as follows

$$f^{(a)} = \begin{cases} 0, \ t \leqslant t_i \\ \left[\frac{1}{2}\left(1 + \sin\left(\pi t/t_a - \pi/2\right)\right)\right]^{3.5}, \ t \leqslant t_i + t_a \\ 1, \ t \leqslant t_i + t_d \\ 0, \ t > t_i + t_d \end{cases},$$

where the activation signal peak-value time is set equal to $t_a = 0.5\,\text{sec}$, while t_i, t_d are the initialization and duration time of the activation function, respectively.

As seen in Subsection 3.1, the squid arm extends if all transverse muscles are activated simultaneously. However, in order for the octopus arm to perform a bending maneuver, primarily longitudinal muscles have to be activated (Liang et al. 2006). To this end, it is assumed that one subregion (group) of longitudinal muscles is activated uniformly ($t_i = 0$); or it is assumed that the same muscle group is activated non-uniformly ($t_i = \bar{z}$), where $\bar{z}$ is the normalized axial position of a material point within the undeformed arm muscular hydrostat. Non-uniform activation occurs due to the variable t_i in respect with the axial position of a muscle fiber material point. The time duration of the activation level is set equal to $t_d = 1\,\text{sec}$.

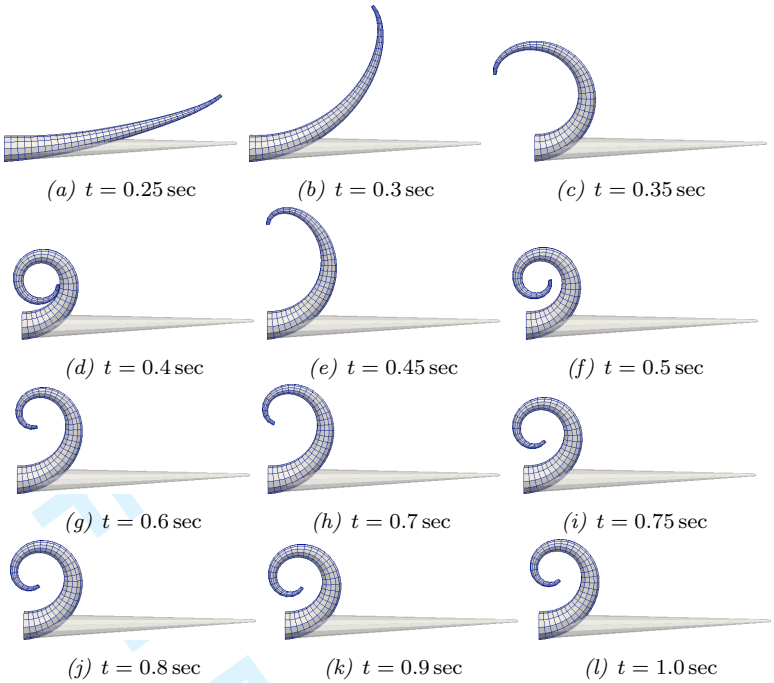

Figure 6. Various snapshots of the octopus arm deformation for uniform activation of one longitudinal muscle group.

Successive snapshots of the arm deformation are presented in Fig. 6, where the transparent grey area corresponds to the undeformed octopus arm. As it can be seen from this figure, the octopus arm performs the bending maneuver within 0.5 sec of full activation level and then it oscillates slightly to this equilibrium position until simulation termination. It is important here to note that no external forces are considered in the present analysis, such as hydrodynamic forces exerted by the surrounding water (Yekutieli et al. 2005; Kazakidi et al. 2011). However, these features can be easily taken into account within the present formulation.

Next, various snapshots of the octopus arm bending procedure are presented in Fig. 7, where non-uniform activation of one longitudinal muscle group takes place. As expected, the arm deforms slowly and requires more time to bend than in the uniform activation case. This is explained by the fact that until 0.25 sec simulation time the first quarter of the longitudinal subregion is fully activated (from $z = 0$ up to 0.025 m), while until 0.5 sec the first half of the longitudinal subregion is fully activated, and so on. We also performed simulations for non-uniform activation of one longitudinal subregion with initialization time $5\bar{z}$ and $2\bar{z}$ (not presented herein) but the arm deformation is rather slow and the final bend is not achieved within 1 sec of simulation time.

The following octopus arm deformation experiment aims at simulating the two primitive arm maneuvers (bending and reaching) in consecutive manner. In order to achieve this maneuver, first a uniform activation ($t_i = 0$) of two neighboring longitudinal muscular groups with activation signal peak-value time $t_a = 0.5$ sec and duration time $t_d = 2$ sec, is enforced. In addition, only a portion of the arm along the z-axis is activated (from $z = 2$ cm up to the tip $z = 10$ cm). Next, the rest two longitudinal muscular zones are activated non-uniformly ($t_i = \bar{z}$) with a time-lag, having activation signal peak-value time at $t_a = 1.5$ sec and duration time $t_d = 2.5$ sec. The activation signals applied on the two groups of the longitudinal muscles are depicted in Fig. 8.

In Fig. 9, various representative snapshots of the octopus arm deformation during the bending and reaching maneuver are presented in successive order. As seen from Figs. 9(a)-9(d), the first two longitudinal muscle groups are activated, thus,

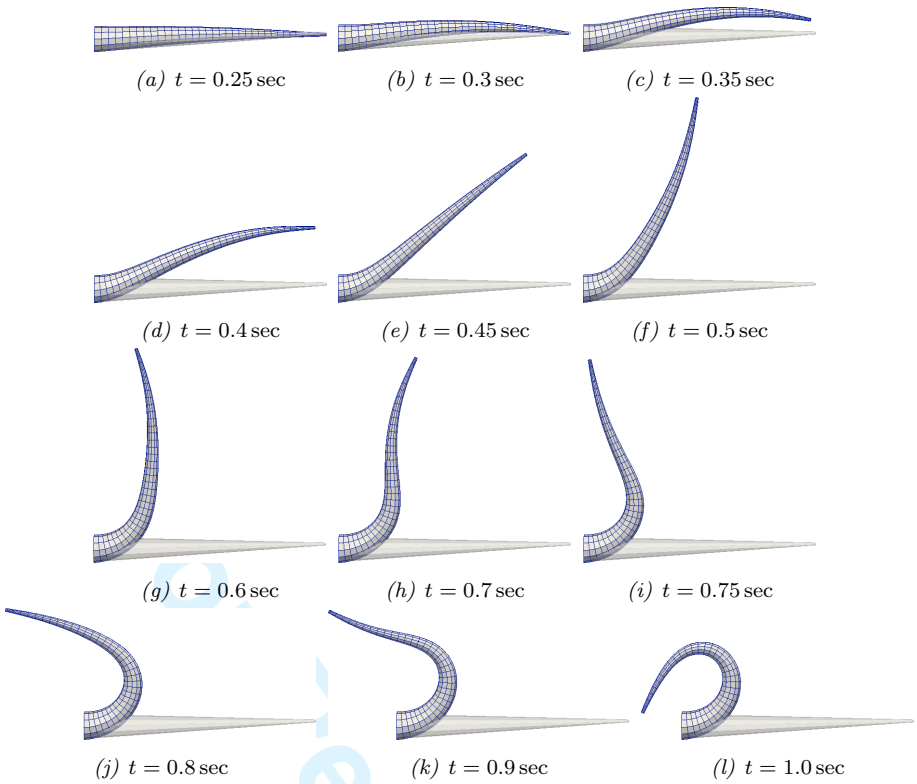

Figure 7. Various snapshots of the octopus arm deformation for non-uniform activation of one longitudinal muscle group.

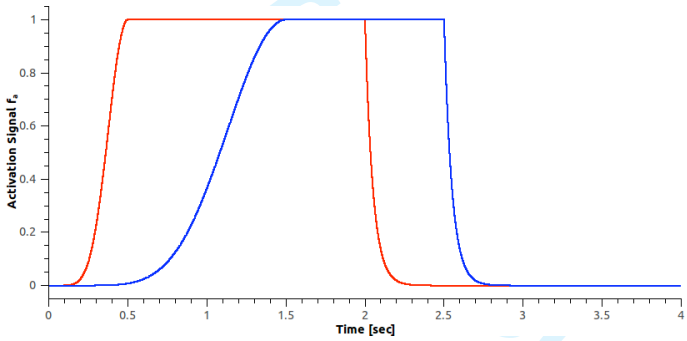

Figure 8. Activation signals occurring for the two groups of longitudinal muscles.

resulting into the arm bending depicted in these figures. However, the bend shape of the arm is less pronounced in this case, as compared to the previous simulation example (see Fig. 6(l)) because 80% of the arm longitudinal muscles are active. In addition, due to the lack of damping in the mechanical non-linear system, the arm exhibits some oscillation from 0.7 sec up to 1 sec. Furthermore, the contraction of the rest longitudinal muscles results into the oscillation decrease and further to arm bending on the opposite direction, since the latter group of muscles is activated all along the arm. This is also evident from Figs. 9(e)-9(q), where a rather slow bend occurs since non-uniform activation is applied to the other two longitudinal muscles. In conjuction with Fig. 8 and Figs. 9(l)-9(q), it can be seen that the activation of the second group of longitudinal muscles and the deactivation of the first group provides a similar hook-like arm deformation (compare Figs. 9(c), 9(p)). Finally, in Figs. 9(q)-9(x) it can be seen the gradual recovery of the octopus arm to its undeformed shape, due to the deactivation of the second group of longitudinal muscles. It is important to note that the reader should not get confused from Fig. 8, where $t_d = 2.5$ sec since the deactivation of this group of muscles is non-

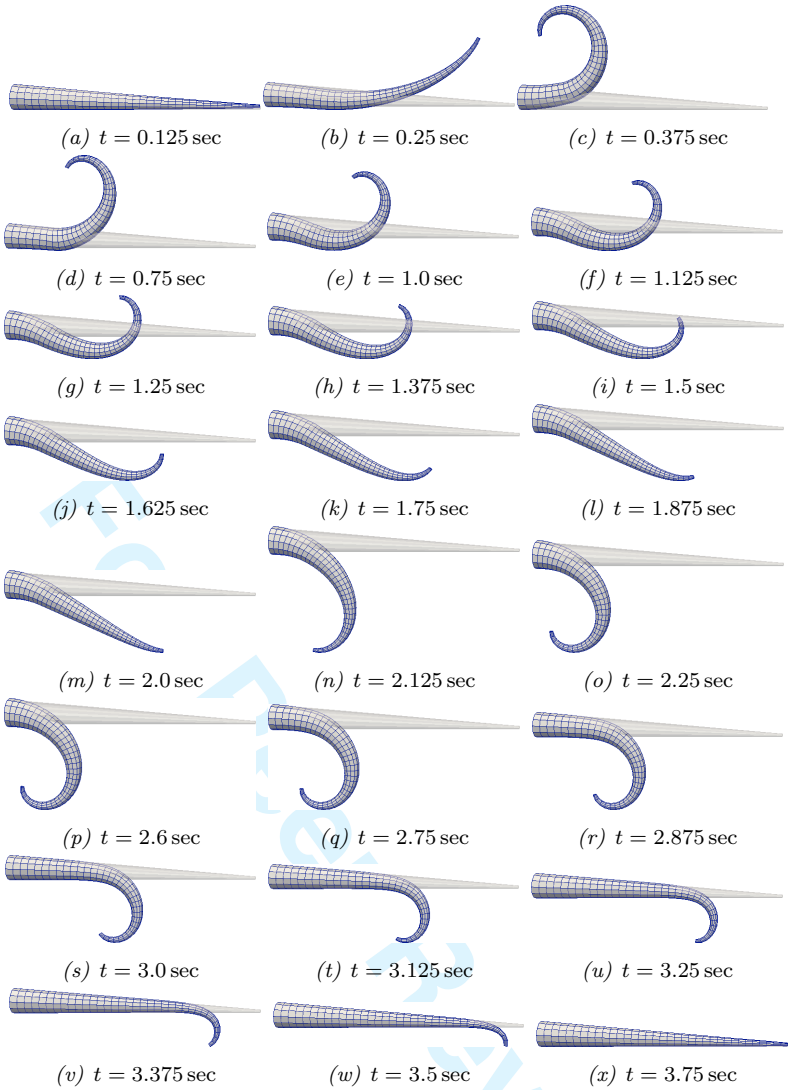

Figure 9. Various snapshots of the octopus arm deformation during the bending and reaching maneuver.

uniform; thus, the true time-duration of the activation signal before decay is equal to $t_i + t_d = \bar{z} + 2.5$ sec.

The final octopus arm deformation experiment involves the simulation of an off-plane bending arm maneuver. Since circumferential muscles were not taken into account in the present work, one way to achieve torsion to the arm is to enforce the stimulation of two neighboring longitudinal muscular groups by applying a proper time-lag. More precisely, the first muscular group is activated non-uniformly ($t_i = \bar{z}$) with activation signal peak-value time $t_a = 0.5$ sec, as in the first example in this subsection, while the second muscular group is activated non-uniformly ($t_i = \bar{z}$) but only a small portion along the z-axis of the arm (from the root $z = 0$ up to $z = 3$ cm) is active.

In Fig. 10, various representative snapshots of the octopus arm deformation during the off-plane bending are presented in successive order until maneuver termination. As it can be seen from Figs. 10(a)-10(l), the arm follows a deformation path identical to the first example demonstrated in this subsection, where non-uniform activation of a single longitudinal muscle group occurs. However, after full activation of the neighbor muscle at 1 sec, the arm seems to exhibit some twisting effects (see Figs. 10(m)-10(x)), which are more pronounced at $t = 1.125$ sec (see Fig. 10(r)). As in the previous example, due to the fact that no damping mech-

anisms were considered into the mathematical model, the deformed arm exhibits some oscillations within $t = 1.5 - 1.9\,\text{sec}$ at the late stage of the maneuver termination. It is important to note here, that if circumferential muscles were considered in the FEM simulations, it would be expected for the arm to achieve significant torsional maneuvers, where the contraction of these helically aligned muscles would also result into arm elongation.

4. Conclusions

In this paper, a non-linear dynamic finite element procedure for simulating biological muscle mechanics is presented. The proposed numerical method is capable of simulating the dynamic mechanical behavior of 3D non-linear nearly incompressible hyperelastic materials –such as muscular hydrostats– that undergo large displacements and deformations. The continuous medium of a muscle is considered to consist of fibers and connective tissues. The former part is described through a Mooney-Rivlin constitutive model, while the latter part is considered to be the sum of active and passive stresses. The non-linear equations of dynamic equilibrium are solved via the Newton-Raphson procedure and implicit time integration is performed through the Newmark method. The validity of the proposed methodology is demostrated with two representative numerical examples, whereas the efficiency and ability of the FEM to simulate octopus arm maneuvers is demonstrated through a series of numerical simulations. The proposed methodology can successfully simulate primitive arm motions of muscular hydrostats more effieciently, compared to previous approaches (Johansson et al. 2000; Yekutieli et al. 2005; Liang et al. 2006). In future developements, oblique muscles of the octopus arm could be accounted for, and introduction of external hydrodynamic forces during the arm movement could allow to produce more realistic simulations. In addition, utilization of higher order elements and p-adaptive procedures could help to increase the accuracy of simulated transient motions.

Acknowledgement

The authors gratefully acknowledge the support by the OCTOPUS IP project with number FP7-231608.

Appendix A. Finite Element linearization steps

Applying the proper transformations to Eq. 7 as discussed in Subsection 2.3 the virtual work variational balance equation can be expressed into the reference configuration as

$$\delta\Pi = \int_{{}_0V} \delta L_{ij}\,\sigma_{ij}\,J\,dV - \int_{{}_0S_T} \delta v_i\,\bar{t}_i\,J_\gamma\,dS = 0\,, \tag{A1}$$

where for simplicity we have removed the inertia domain integral of Eq. 7

Inserting into Eq. A1 proper finite element interpolation polynomials, where unknown kernel quantities are interpolated via Lagrange polynomial bases: ${}_0x_i = \sum_\alpha N^{(\alpha)}\,{}_0x_i^{(\alpha)}$, $\partial u_i/\partial\,{}^t x_j = \sum_\alpha \left(\partial N^{(\alpha)}/\partial\,{}^t x_j\right) u_i^{(\alpha)}$, and given that the virtual velocity

gradient matrix can be written in the form: $\delta L_{ij} = {}^{\partial \delta v_i}/_{\partial^t x_j} = \left({}^{\partial \delta v_i}/_{\partial_0 x_k}\right) F^{-1}_{kj}$, it follows that

$$\left\{ \int_{{}_0V} \frac{\partial N^{(\alpha)}}{\partial^t x_j}\, \sigma_{ij}\, J\, dV - \int_{{}_0S_T} N^{(\alpha)}\, \bar{t}_i\, J_\gamma\, dS \right\} \delta v_i^{(\alpha)} = 0 \Leftrightarrow$$

$$\left\{ \int_{{}_0V} \frac{\partial N^{(\alpha)}}{\partial_0 x_k}\, F^{-1}_{kj}\, \sigma_{ij}\, J\, dV - \int_{{}_0S_T} N^{(\alpha)}\, \bar{t}_i\, J_\gamma\, dS \right\} \delta v_i^{(\alpha)} = 0\,. \qquad \text{(A2)}$$

In order to solve the above discrete non-linear virtual work equation using the Newton-Raphson procedure, it is assumed a corrected updated solution $u_i^{(\alpha)} + \Delta u_i^{(\alpha)}$, where $u_i^{(\alpha)}$ the solution at the end of the preceding time increment or the previous iteration solution. Given the fact that no follower external forces are present in the current analysis, Eq. A2 becomes

$$\int_{{}_0V} \frac{\partial N^{(\alpha)}}{\partial_0 x_k}\, [F + \Delta F]^{-1}_{kj}\, \sigma_{ij}(u + \Delta u)\, J\, dV = 0\,, \qquad \text{(A3)}$$

where the Cauchy stress tensor and the deformation gradient determinant J are dependent to that increment.

The linearization of the above integral quantities are given below in brief:

$$[F + \Delta F]^{-1}_{kj} \approx F^{-1}_{kj} - F^{-1}_{km} \frac{\partial F_{mn}}{\partial u_l} F^{-1}_{nj}\, \Delta u_l = F^{-1}_{kj} - F^{-1}_{kl} \frac{\partial N^{(\beta)}}{\partial_0 x_r} F^{-1}_{rj}\, \Delta u_l^{(\beta)}\,, \qquad \text{(A4)}$$

$$\sigma_{ij}\, J \approx \sigma_{ij}\, J + \frac{\partial (\sigma_{ij} J)}{\partial F_{kl}} \frac{\partial F_{kl}}{\partial u_s}\, \Delta u_s = \sigma_{ij}\, J + \frac{\partial (\sigma_{ij} J)}{\partial F_{kl}} \frac{\partial N^{(\beta)}}{\partial_0 x_l}\, \Delta u_k^{(\beta)}\,, \qquad \text{(A5)}$$

with ${}^{\partial J}/_{\partial F_{pq}} = J F^{-1}_{qp}$. Inserting the linearizations of Eqs. A4 and A5 into Eq. A3 it is obtained

$$\left\{ \int_{{}_0V} \left[\left(\frac{\partial \sigma_{ij}}{\partial F_{kl}} + \sigma_{ij} F^{-1}_{kl} \right) \frac{\partial N^{(\alpha)}}{\partial_0 x_r} F^{-1}_{rj} \frac{\partial N^{(\beta)}}{\partial_0 x_l} - \sigma_{ij} \frac{\partial N^{(\alpha)}}{\partial_0 x_m} F^{-1}_{mk} \frac{\partial N^{(\beta)}}{\partial_0 x_n} F^{-1}_{nj} \right] J\, dV \right\} \Delta u_k^{(\beta)}$$

$$= \int_{{}_0S_T} N^{(\alpha)}\, \bar{t}_i\, J_\gamma\, dS - \int_{{}_0V} \sigma_{ij} \frac{\partial N^{(\alpha)}}{\partial_0 x_p} F^{-1}_{pj}\, J\, dV\,, \qquad \text{(A6)}$$

or equivalently

$$\left\{ \int_{{}_0V} \left[C_{ijkl} \frac{\partial N^{(\alpha)}}{\partial_0 x_r} F^{-1}_{rj} \frac{\partial N^{(\beta)}}{\partial_0 x_s} F^{-1}_{sl} - \sigma_{ij} \frac{\partial N^{(\alpha)}}{\partial_0 x_m} F^{-1}_{mk} \frac{\partial N^{(\beta)}}{\partial_0 x_n} F^{-1}_{nj} \right] J \, dV \right\} \Delta u^{(\beta)}_k = \int_{{}_0S_T} N^{(\alpha)} \, \bar{t}_i \, J_\gamma \, dS - \int_{{}_0V} \sigma_{ij} \frac{\partial N^{(\alpha)}}{\partial_0 x_p} F^{-1}_{pj} \, J \, dV \,, \tag{A7}$$

where

$$C_{ijkl} = \frac{\partial \sigma_{ij}}{\partial F_{ks}} F_{ls} + \sigma_{ij} \, \delta_{kl} \,. \tag{A8}$$

From Eq. A7, after some algebra, it can be obtained the matrix semi-discrete form of Eq. 8.

Appendix B. Tangent stiffness matrix and stress tensor evaluation

As discussed in Section 2, the Cauchy stress distribution of biological muscles is considered equal to: $\sigma_{ij} = \sigma^{(ct)}_{ij} + \sigma^{(f)}_{ij}$. Therefore, it can be safely assumed that the material tangent stiffness matrix in the finite element level is equal to the sum of the corresponding ones of the connective tissues and fibers

$$C_{ijkl} = \frac{\partial \sigma_{ij}}{\partial F_{ks}} F_{ls} + \sigma_{ij} \, \delta_{kl} = C^{(ct)}_{ijkl} + C^{(f)}_{ijkl} \,. \tag{B1}$$

The fourth-order material tangent stiffness tensor of the connective tissues can be evaluated analytically, given the corresponding expression of the Cauchy stress tensor (see Eq. 4), and is provided below

$$\begin{aligned} C^{(ct)}_{ijkl} = {} & \left[{}^4\!/_{9J} \left(c_1 \bar{I}_1 + 4 c_2 \bar{I}_2 \right) + K(2J-1) \right] \delta_{ij} \delta_{kl} \\ & - {}^4\!/_3 \left(c_1 + 2 c_2 \bar{I}_1 \right) J^{-5/3} \left(B_{ij} \delta_{kl} + \delta_{ij} B_{kl} \right) + {}^8\!/_3 \, c_2 J^{-7/3} \left(B^2_{ij} \delta_{kl} + \delta_{ij} B^2_{kl} \right) \\ & + 2 (c_1 + c_2 \bar{I}_1) J^{-5/3} \left(\delta_{ik} B_{jl} + B_{il} \delta_{jk} \right) - 2 c_2 J^{-7/3} \left(\delta_{ik} B^2_{jl} + B^2_{il} \delta_{jk} \right) \\ & + 2 c_2 J^{-7/3} \left(2 B_{ij} B_{kl} - B_{il} B_{jk} - B_{ik} B_{jl} \right) \,, \end{aligned} \tag{B2}$$

where $B^2_{ij} = B_{ik} B_{kj}$.

For the fiber part, the Cauchy stress tensor is defined as $\sigma^{(f)}_{ij} = \sigma^m_0 \, (1 + \varepsilon^m_0) \, \hat{m}_i \hat{m}_j$. Given the fiber stress expressions (see Eqs. Eqs. 5 and 6), the analytical expression for the muscle fibers material tangent stiffness tensor can be derived

$$C^{(f)}_{ijkl} = \left(\lambda \frac{\partial \sigma^m}{\partial \varepsilon^m_0} - 2\sigma^m\right) \hat{m}_i \hat{m}_j \hat{m}_k \hat{m}_l + \sigma^m \left(\hat{m}_i \hat{m}_j \delta_{kl} + \delta_{ij} \hat{m}_k \hat{m}_l + \delta_{ik} \hat{m}_j \hat{m}_l + \hat{m}_i \delta_{jk} \hat{m}_l\right) , \tag{B3}$$

where $\sigma^m = \sigma^m_0(1+\varepsilon^m_0)$. The derivative of the fiber nominal stress in respect with the nominal strain ε^m_0 is given explicitly

$$\frac{\partial \sigma^m_0}{\partial \varepsilon^m_0} = \frac{\partial \sigma^{(pass)}}{\partial \varepsilon^m_0} + \sigma^{(max)} f^{(a)} \left(\frac{\partial f^{(l)}}{\partial \varepsilon^m_0} f^{(v)} + f^{(l)} \frac{\partial f^{(v)}}{\partial \dot{\varepsilon}^m_0} \frac{1}{\Delta t}\right) . \tag{B4}$$

In the previous equation it is assumed that the nominal strain rate is approximately equal to $\dot{\varepsilon}^m_0 \approx \Delta \varepsilon^m_0 / \Delta t$; therefore, the quantity $\partial f^{(v)} / \partial \varepsilon^m_0$ by chain differentiation is set equal to $(\partial f^{(v)} / \partial \dot{\varepsilon}^m_0)/\Delta t$.

On the above calculations, the following differentiation identities are utilized:

$$\frac{\partial \lambda}{\partial F_{km}} = \frac{1}{\lambda} \left(F_{kr} \hat{n}_r\right) \hat{n}_m = \hat{m}_k \hat{n}_m , \tag{B5}$$

$$\frac{\partial \hat{m}_i}{\partial F_{km}} = \frac{1}{\lambda} \delta_{ik} \hat{n}_m - \frac{1}{\lambda^2} \left(F_{is} \hat{n}_s\right) \frac{\partial \lambda}{\partial F_{km}} = \frac{1}{\lambda} \left(\delta_{ik} \hat{n}_m - \hat{m}_i \hat{m}_k \hat{n}_m\right) . \tag{B6}$$

Working in the same manner, one can derive the material tangent stiffness for the classical three-element Hill muscle model. Following the same notation as in (Tang et al. 2007), the Cauchy stress in the fiber level is defined by the relationhip

$$\sigma^{(f)}_{ij} = \frac{1}{J} g \bar{\lambda} \left(\hat{m}_i \hat{m}_j - 1/3 \, \delta_{ij}\right) , \tag{B7}$$

where $\bar{\lambda} = \lambda J^{-1/3}$ and $g\left(\bar{\lambda}\right) = \sigma_0 f_{\text{PEE}} + \beta \, e^{\alpha(\lambda_s - 1)} - \beta$; with σ_0 being the maximum isometric stress, α, β are material parameters, λ_s is the stretch of the Hill series elastic element and f_{PEE} a pre-defined function with respect to $\bar{\lambda}$ for the Hill parallel elastic element component (Tang et al. 2009).

The corresponding fourth-order material tangent stiffness tensor for the Hill muscle model of fibers can be evaluated analytically:

$$C^{(f)}_{ijkl} = \bar{\lambda}/9 \left(g' \bar{\lambda} + g\right) \delta_{ij} \delta_{kl} - \bar{\lambda}/3 \left(g' \bar{\lambda} + g\right) \left(\hat{m}_i \hat{m}_j \delta_{kl} + \delta_{ij} \hat{m}_k \hat{m}_l\right) + \bar{\lambda} \left(g' \bar{\lambda} - g\right) \hat{m}_i \hat{m}_j \hat{m}_k \hat{m}_l + g \bar{\lambda} \left(\delta_{ik} \hat{m}_j \hat{m}_l + \hat{m}_i \delta_{jk} \hat{m}_l\right) , \tag{B8}$$

where $g' = \sigma_0 \left(\partial f_{\text{PEE}} / \partial \bar{\lambda}\right) + \left(\kappa + 1/\kappa\right) \alpha \, \beta \, e^{\alpha(\lambda_s - 1)}$ and κ a parameter relating the fiber stretch λ with the corresponding stretches of the series elastic and the contractile element.

For the frog gastrocenemius muscle deformation problem (Subsection 3.2), the following Cauchy stress distribution definition for the muscle connective tissues is adopted

$$\sigma_{ij}^{(ct)} = 2\,b\,c\,e^{b(\bar{I}_1-3)}J^{-5/3}B_{ij} - \left[(2/3J)\;b\,c\,e^{b(\bar{I}_1-3)}\bar{I}_1 + 2K(1-J)\right]\delta_{ij}\,, \qquad \text{(B9)}$$

where b, c and K are material parameters, according to the work of Tang et al. (2007).

For this case, the tangent stiffness matrix (see Eq. B1) is given analytically by the expression

$$\begin{aligned} C_{ijkl}^{(ct)} = &\left[4/9J\,(b\bar{I}_1+1)\,b\,c\,e^{b(\bar{I}_1-3)}\bar{I}_1 + 2K(2J-1)\right]\delta_{ij}\delta_{kl} \\ &+ 4\,b^2\,c\,e^{b(\bar{I}_1-3)}J^{-7/3}B_{ij}B_{kl} + 2\,b\,c\,e^{b(\bar{I}_1-3)}J^{-5/3}\left(\delta_{ik}B_{jl} + B_{il}\delta_{jk}\right) \\ &- 4/3\,(b\bar{I}_1+1)\,b\,c\,e^{b(\bar{I}_1-3)}J^{-5/3}\left(B_{ij}\delta_{kl} + \delta_{ij}B_{kl}\right)\,. \end{aligned} \qquad \text{(B10)}$$

References

Balay S, Buschelman K, Eijkhout V, Gropp WD, Kaushik D, Knepley MG, Curfman McInnes L, Smith BF, Zhang H. 2008. PETSc Users Manual. Argonne National Laboratory, ANL-95/11 - Revision 3.0.0.

Bowler AF. 2009. Applied Mechanics of Solids. CRC Press.

Fernandez JW, Buist ML, Nickerson DP, Hunter PJ. 2005. Modelling the passive and nerve activated response of the rectus femoris muscle to a flexion loading: A finite element framework. Medical Engineering & Physics 27:862–870.

Fung YC. 1981. Biomechanics: Mechanical Properties of Living Tissues. Springer-Verlag.

Geuzaine C, Remacle J-F. 2009. Gmsh: a three-dimensional finite element mesh generator with built-in pre- and post-processing facilities. International Journal for Numerical Methods in Engineering 79:1309–1331.

Hill AV. 1938. The heat of shortening and the dynamic constants of muscle. Proceedings of the Royal Society of London. Series B, Biological Sciences 126:136–195.

Humphrey JD, Yin FCP. 1987. On constitutive relations and finite deformations of passive cardiac tissue: I. A pseudostrain-energy function. Journal of Biomechanical Engineering 109:298–304.

Huxley AF. 1957. Muscle structure and theories of contraction. Progress in Biophysics & Molecular Biology 164:255–318.

Johansson T, Meier M, Blickhan R. 2000. A Finite-Element Model for the Mechanical Analysis of Skeletal Muscles. Journal of Theoretical Biology 206:131–149.

Kazakidi A, Vavourakis V, Ekaterinaris JA, Tsakiris DP. 2011. Computational investigation of octopus arm hydrodynamics. 4th ANSA & μETA International Conference, Thessaloniki, Greece.

Kier WM, Stella MP. 2007. The arrangement and function of octopus arm musculature and connective tissue. Journal of Morphology 268:831–843.

Kirk B, Peterson JW, Stogner RH, Carey GF. 2006. libMesh: A C++ Library for parallel adaptive mesh refinement/coarsening simulations. Engineering with Computers 22:237–254.

Kojic M, Mijailovic S, Zdravkovic N. 1998. Modelling of muscle behavior by the finite element method using Hill's three-element model. International Journal for Numerical Methods in Engineering 43:941–953.

Liang Y, McMeeking RM, Evans AG. 2006. A finite element simulation scheme for biological muscular hydrostats. Journal of Theoretical Biology 242:142–150.

Lu YT, Zhu HX, Richmond S, Middleton J. 2010. A visco-hyperelastic model for skeletal muscle tissue under high strain rates. Journal of Biomechanics 43:2629–2632.

Martins JAC, Pires EB, Salvado R, Dinis PD. 1998. A numerical model of passive and active behavior of skeletal muscles. Computer Methods in Applied Mechanics and Engineering 151:419–433.

Martins JAC, Pato MPM, Pires EB. 2006. A finite element model of skeletal muscles. Virtual and Physical Prototyping 1:159–170.

Mooney M. 1940. A theory of large elastic deformation. Journal of Applied Physics 11:582–592.

Nigg BM, Herzog W. 1999. Biomechanics of the musculo-skeletal system, 2nd ed. Wiley.

Oomens CWJ, Maenhout M, Van Oijen CH, Drost MR, Baaijens FP. 2003. Finite element modelling of contracting skeletal muscle. Philosophical Transactions of the Royal Society B: Biological Sciences 358:1453–1460.

Röhrle O, Pullan AJ. 2007. Three-dimensional finite element modelling of muscle forces during mastication. Journal of Biomechanics 40:3363–3372.

Stojanovic B, Kojic M, Rosic M, Tsui CP, Tang CY. 2007. An extension of Hill's three-component model to include different fiber types in finite element modeling of muscle. International Journal for Numerical Methods in Engineering 71:801–817.

Tang CY, Tsui CP, Stojanovic B, Kojic M. 2007. Finite element modelling of skeletal muscles coupled with fatigue. International Journal of Mechanical Sciences 49:1179–1191.

Tang CY, Zhang G, Tsui CP. 2009. A 3D skeletal muscle model coupled with active contraction of muscle fibres and hyperelastic behavior. Journal of Biomechanics 42:865–872.

Van Leeuwen JL. 1991. Optimum power output and structural design of sarcomeres. Journal of Theoretical Biology 149:229–256.

Van Leeuwen JL, Kier WM. 1997. Functional design of tentacles in squid: linking sarcomere ultrastructure to gross morphological dynamics. Philosophical Transactions of the Royal Society B: Biological Sciences 352:551–571.

Yekutieli Y, Sagiv-Zohar R, Aharonov R, Engel Y, Hochner B, Flash T. 2005. Dynamic model of the octopus arm. I. Biomechanics of the octopus reaching movement. Journal of Neurophysiology 94:1443–1458.

Zajac FE. 1989. Muscle and tendon: Properties, models, scaling and application to biomechanics and motor control. CRC Critical Reviews in Biomedical Engineering 17:359–411.

Zienkiewicz OC, Taylor RL. 2005. The Finite Element Method for Solid and Structural Mechanics, 6th ed. Elsevier Butterworth-Heinemann.

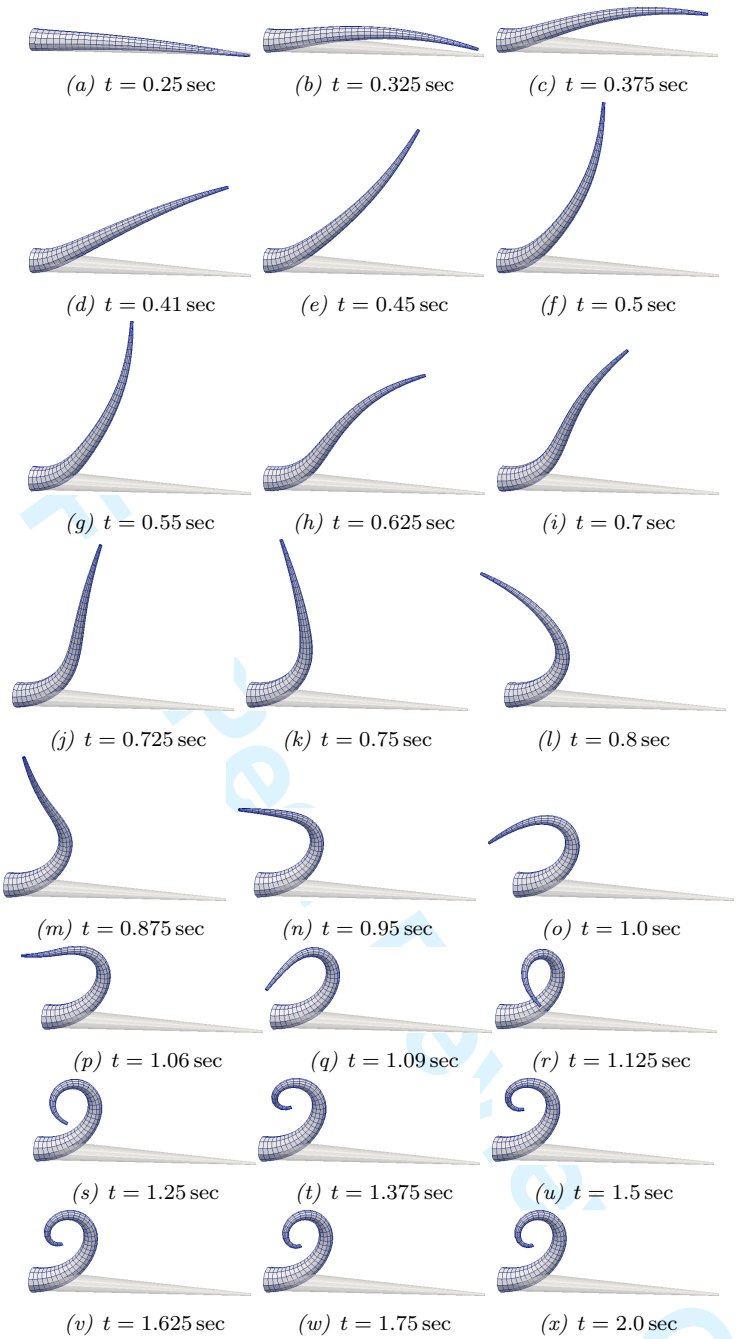

Figure 10. Various snapshots of the octopus arm deformation during an off-plane bending maneuver.